

RSC Advances



This is an *Accepted Manuscript*, which has been through the Royal Society of Chemistry peer review process and has been accepted for publication.

Accepted Manuscripts are published online shortly after acceptance, before technical editing, formatting and proof reading. Using this free service, authors can make their results available to the community, in citable form, before we publish the edited article. This *Accepted Manuscript* will be replaced by the edited, formatted and paginated article as soon as this is available.

You can find more information about *Accepted Manuscripts* in the [Information for Authors](#).

Please note that technical editing may introduce minor changes to the text and/or graphics, which may alter content. The journal's standard [Terms & Conditions](#) and the [Ethical guidelines](#) still apply. In no event shall the Royal Society of Chemistry be held responsible for any errors or omissions in this *Accepted Manuscript* or any consequences arising from the use of any information it contains.

Structural Prediction, Analysis and Decomposition Mechanism of Solid $M(\text{NH}_2\text{BH}_3)_n$ (M=Mg, Ca and Al)

**Kun Wang^{a,b}, Vaida Arcisauskaitė^b, Jian-She Jiao^c, Jian-Guo Zhang^{*a}, Tonglai Zhang^a,
Zun-Ning Zhou^a**

^aState Key Laboratory of Explosion Science and Technology, Beijing Institute of Technology, Beijing 100081 P. R. China

^bDepartment of Chemistry, Inorganic Chemistry Laboratory, University of Oxford, South Parks Road, Oxford OX1 3QR, United Kingdom

^cResearch Institute of FA and ADA Equipment and Technology, General Armament Department, Beijing 100012

* The type of article: Research paper

Corresponding authors: Jian-Guo Zhang, Tel & Fax: +86 10 68913818.

E-mail: zjgbit@bit.edu.cn & kun.wang@chem.ox.ac.uk

Abstract: Multivalent Metal amidoboranes (MABs) are considered to be the important candidates for hydrogen storage materials. Whereas CaAB crystal structure has been determined experimentally, the crystal structures of MgAB and AlAB have not been obtained, thus hindering the further development of MABs. In this work, we determine the crystal and electronic structures of MABs (M=Mg, Ca, Al), obtain their phononic density of states and thermodynamic properties. By means of M-N population analysis, we conclude that Al-N and Ca-N bonds have a covalent character whereas Mg-N bond - ionic. We furthermore observe that HOMO-LUMO gaps and thus stability follows the trend $\text{MgAB} \approx \text{AlAB} > \text{CaAB}$. Thermodynamic properties and their dependence on temperature seem to be very similar for AlAB and MgAB compounds compared to CaAB. CaAB has the lowest enthalpy and thus the lowest internal energy in the series of MABs (M=Mg, Ca, Al). We also propose most probable dehydrogenation pathways during which $4n$ H_2 molecules are released (in 4 steps) from MgAB and CaAB and $6n$ H_2 (in 6 steps) from AlAB indicating that dehydrogenation from the same AB group twice in a row is less likely to occur. Furthermore, we reveal that the energy barriers for the 1st dehydrogenation step follow the trend $\text{CaAB} > \text{MgAB} > \text{AlAB}$. This is agreement with the experiments showing that AlAB will start dehydrogenate at the lowest temperature followed by MgAB. Finally, we propose that complete dehydrogenation rates at 400 °C follow the trend $\text{MgAB}(1.73 \times 10^{-14} \text{ min}^{-1}) \approx \text{CaAB}(1.72 \times 10^{-14} \text{ min}^{-1}) > \text{AlAB}(2.18 \times 10^{-16} \text{ min}^{-1})$.

Keywords: hydrogen-storage dehydrogenation Multivalent Metal amidoboranes
Monte-Carlo simulation first-principle study

1. Introduction

Studies of ammonia-borane (AB) compounds have demonstrated that AB is a source of chemically stored hydrogen and can meet DOE (Department of Energy, USA) performance parameters except that it is an irreversible reaction¹⁻⁹. It has also been found that by replacing one of the hydrogen atoms in AB with a metal (M), the compound displays further interesting characteristics¹⁰⁻¹⁶ such as a change in the decomposition path and a decrease in the decomposition temperature. MABs (LiAB, NaAB, CaAB, MgAB, AlAB) start releasing their hydrogen at approximately 50 – 90 °C^{15,17-20}, whereas AB start releasing their hydrogen only at around 150 °C. Furthermore, dehydrogenation in MABs is less exothermic than in ABs, which is beneficial when looking for a reversible reaction^{15,17}. Finally, MABs are environmentally friendly, safe and stable compounds^{21,22}.

Investigation of MABs ($M(\text{NH}_2\text{BH}_3)_n$), where M is a univalent metal ion has centred on the alkali metals such as Li, Na, and K, owing to their low mass, simple electronic structure, and minimal effect on the content of hydrogen in the molecules²³⁻²⁶. Both, experimental and computational studies on MABs, where M is a multivalent metal ion (such as Mg^{19,27-29}, Ca^{25,28-30}, Sr¹⁰, Al³¹, and Y³²) have all also been performed and we summarized the results of these studies in Ref. 22. Many different properties of MABs have been discovered due to the large radius of these multivalent metal ions. Whereas CaAB crystal structure has been determined²⁵ experimentally using single crystal XRD, the crystal structures of MgAB and AlAB¹⁸ have not been determined, thus hindering the further development of MABs. For the MgAB the data from powder XRD is available¹⁹.

The present work has three major objectives. First, we aim to simulate the crystal structures of MgAB and AlAB using the Monte Carlo (MC) packing algorithm within the MS Polymorph code³³. Our second objective is to optimize the crystal structures of CaAB (obtained from single crystal XRD), MgAB and AlAB (obtained from our MC simulations) and then calculate the electronic structure, phononic density of states and thermodynamic properties for these compounds using the first principles methodologies within the MS CASTEP code³⁴. Finally, we aim to determine the mechanism of decomposition (pathways and their potential energy surfaces) using *ab initio* methodologies within the Gaussian 09³⁵ program package similarly to our previous studies on some univalent metal amidoboranes^{36,37}.

2. Computational methods

The prediction of crystal structure of MgAB and AlAB was done using the Monte Carlo (MC) packing algorithm within the MS Polymorph code³³. The input molecular structures for these MC packing simulations were built and optimized with the B3LYP/6-311++G(3d,2p)³⁸⁻⁴⁰ methodology using Gaussian 09 program package³⁵.

MC packing algorithm follows a simulated annealing procedure intended to search for the lowest minima of the energy function E of molecular crystals. The determination of space groups is based on the principle pointed out by Belsky⁴¹. In our MC simulations we used the universal force field (UFF)⁴² to calculate the energy and a geometry of our systems. The motion parts in our MC prediction were chosen to be metal cations and rigid units of $[\text{NH}_2\text{BH}_3]^-$ which were allowed to rotate and translate. The temperature range of annealing was set from 300 to 3×10^5 K. Further computational details of these MC simulations are listed in the [supporting material, S1](#).

The optimized geometries of MAB (M = Ca, Mg, Al) crystals and their electronic structure (partial density of states), phononic density of states and thermodynamic properties (Phonons module) were obtained using the combination of Density Functional Theory^{43, 44} (DFT) and the projector augmented wave methodology (PAW)⁴⁵, which is implemented in the CASTEP code³⁴. The generalized gradient approximation⁴⁶ of Perdew, Burke and Erzerhof⁴⁷ (GGA-PBE) for the exchange-correlation function was used throughout the CASTEP calculations. The Vanderbilt-type ultrasoft pseudopotentials⁴⁸ with valence states $2p^63s^2$ for Mg, $3s^23p^64s^2$ for Ca, $3s^23p^1$ for Al, $2s^22p^1$ for B, $2s^22p^3$ for N, and $1s^1$ for H were used to describe the core electrons. A plane wave basis set with an energy cutoff of 450 eV was used. The Brillouin-zone integration of CaAB, MgAB and AlAB was done by using $3 \times 3 \times 3$, $2 \times 4 \times 2$ and $1 \times 2 \times 1$ Monkhorst-Pack meshes⁴⁹, respectively. Structural relaxations of atomic positions, cell parameters and volume during geometry optimization were carried out by the BFGS method⁵⁰ until the residual forces and stresses were smaller than $0.005 \text{ eV}/\text{\AA}$ and 0.05 Gpa, respectively. Phononic density of states and thermodynamic properties for optimized structures were obtained using the finite displacement method within the Phonons module. This method proceeds by shifting each atom by a small amount, then performing a Self Consistent Field calculation to evaluate the forces on the perturbed configuration. In Phonon calculations the cutoff radius of the supercells for each crystal was set to 4\AA .

For the optimized crystal structures of CaAB and MgAB we calculated the XRD using the Reflex code⁵¹ in Materials Studio and compared it to the experimentally determined single crystal

and powder XRD data^{19,25}, respectively. Such a comparison is useful when predicting the structure of crystals.

The kinetic study of dehydrogenation was performed on MABs in gas phase using the Gaussian 09 program³⁵ package. The input molecular MAB structures for the stationary points were taken from our CASTEP study described above. All possible structures in the reaction pathway were optimized without constraints with DFT (B3LYP functional)^{39,40} and 6-311++G(3d,2p) basis set. Frequency calculations at the same level of theory were also performed to identify all of the stationary points (zero imaginary frequencies) or transition states (one imaginary frequency). Intrinsic reaction coordinates (IRC) were calculated for the transition states to confirm that such structures indeed connect two relevant minima. The rate of dehydrogenation was calculated using the conventional transition state theory. Finally, for our obtained stationary and transition states we calculated the potential energy curve with the CCSD(T)⁵²/6-311++G(3d,2p).

3. Results and Discussions

3.1 Structural properties and HOMO-LUMO energy of crystal MABs

The crystal structures of MABs predicted by MC packing algorithm (MgAB and AlAB) or single crystal XRD (CaAB) and then optimized with DFT using CASTEP are illustrated in Fig. 1. The internal coordinates and lattice constants of CaAB, MgAB and AlAB are presented in the supporting material (Table S1 – S3). For CaAB and MgAB we used the monoclinic space group C2 determined by single crystal²⁵/powder experiments¹⁹, respectively. For the optimized crystal structures we calculated the XRD which compared reasonably to the experimentally determined single and powder XRD data (Fig. S1 in the supporting material).

In crystalline MgAB each Mg²⁺ is coordinated to two [NH₂BH₃]⁻ groups through N (d(Mg-N)=2.123 Å, ∠(N-Mg-N)=102.1°) and to two other [NH₂BH₃]⁻ groups through B (d(Mg-B) = 2.487 Å, ∠(N-Mg-B)=108.8°) forming a tetrahedral structure similar to that of Na₂Mg(NH₂BH₃)₄⁵³. In crystalline CaAB, each Ca²⁺ directly bonds to two [NH₂BH₃]⁻ anions through N (d(Ca-N)=2.480 Å, ∠(N-Ca-N)=161.1°) and coordinates to four further lying [NH₂BH₃]⁻ anions through B. Our calculations revealed that crystal AlAB adopts orthorhombic symmetry in space group Pbcn. Each Al³⁺ ion is coordinated by three [NH₂BH₃]⁻ anions through N related by a C3 rotation axis. Al³⁺ is also coordinated to one further [NH₂BH₃]⁻ anion through B, which lies on the aforementioned C3 axis. Hence a tetrahedral coordination environment is observed with C3v

point group symmetry. The bond lengths of AlAB are listed in Table 1. The reported structural parameters of CaAB and MgAB are in an agreement with the experimentally (CaAB: Ref. 25 ESI) and computationally (CaAB: Ref. 25, 28, 30 and MgAB: Ref. 28) determined ones as shown in Table 1 and the supporting material (Table S4).

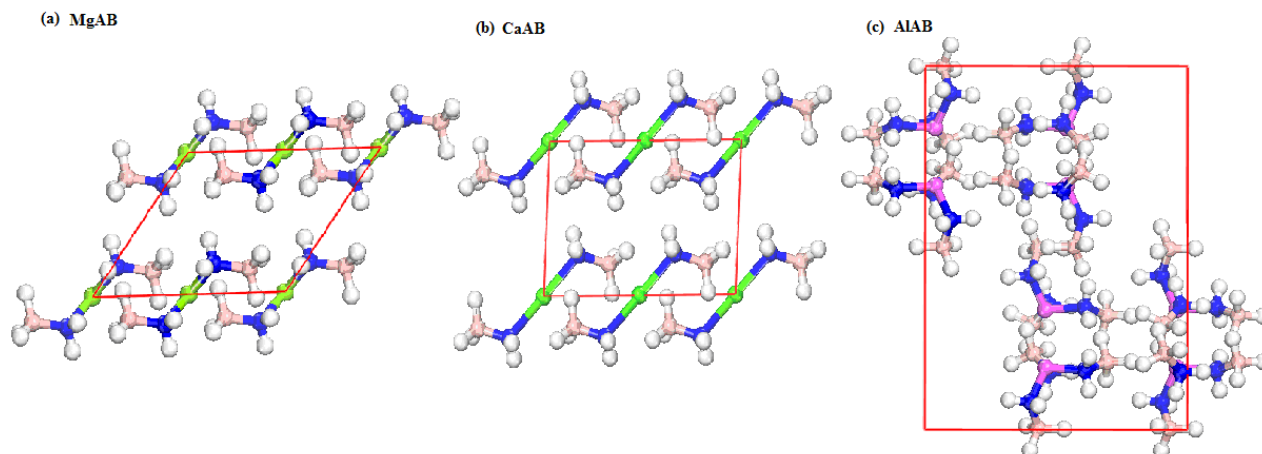


Fig.1 Crystal structures of the MABs (M=Mg, Ca, Al). The structures are shown in a bond-stick view, and the viewing directions shown are (a) [010], (b) [100], and (c) [010]. The green, purple, blue, pink and white spheres denote Mg, Ca, Al, N, B and H atoms, respectively.

Table 1 The calculated populations, bond lengths (Å), HOMO-LUMO gap energies (eV) and band gaps (eV) of MABs.

	MgAB		CaAB		AlAB	
	Population	Bond length	Population	Bond length ^a	Population	Bond length
M-N ^a	0	2.123	0.14	2.480 (2.452)	0.43	1.906
N-B	0.63	1.556	0.64	1.547 (1.547)	0.57	1.565
N-H	0.76	1.033	0.72	1.031/1.031 (1.022/1.027)	0.71	1.033
B-H	1.02	1.218	0.93	1.231/1.243/1.249 (1.243/1.245/1.251)	1.02	1.200
H ^{δ+} ... ^{δ-} H	-	2.632	-	2.771	-	2.625
E _{HOMO-LUMO}		5.3		4.2		5.2
Band gap		5.0		3.8		5.2

a: For CaAB, the values in the brackets are the experimental results²⁵.

The bonding types can be predicted by looking at the electronic populations. As the population for Mg-N bond is 0, no electrons seem to be shared between Mg and N, which indicates that Mg-N bond is a pure ionic bond. Instead, the populations for Ca-N and Al-N bonds are 0.14 and 0.43, respectively, indicating a covalent character of these bonds, in particular, Al-N.

In order to explain such a bonding trend, we have looked at the radii of the metal cations ($R_{\text{Mg}^{2+}} = 72 \text{ pm}$, $R_{\text{Ca}^{2+}} = 100 \text{ pm}$, $R_{\text{Al}^{3+}} = 54 \text{ pm}$), electronegativity values (1.31 for Mg, 1.0 for Ca, 1.61 for Al) and M-N bond lengths ($d(\text{Mg-N})=1.906 \text{ \AA}$, $d(\text{Ca-N})=2.480 \text{ \AA}$, $d(\text{Al-N})=1.906 \text{ \AA}$). The ionic radius of Mg^{2+} is similar to that of Li^+ ($R_{\text{Li}^+} = 76 \text{ pm}$), but the charge is twice as large. Due to the steric hindrance of $[\text{NH}_2\text{BH}_3]^-$ groups, it could be difficult to compensate for the positive charge of Mg^{2+} and this could explain the reason why the successful synthesis of single crystal MgAB has not been reported so far. The ionic radius of Ca^{2+} is larger than the ionic radius of Mg^{2+} and this explains the trend of observed populations for Mg-N and Ca-N bonds, 0 and 0.14, respectively. On one hand, the ionic radius of Al^{3+} is smallest of all, but on the other hand the Al-N bond length is shortest of all, and the electronegativity is largest of all, thus resulting in the largest M-N bond population (0.43). The B-N bond is the weakest in the Al-AB system probably due to the fact that Al is most electronegative of all Ms. One could thus expect massive impurity of ammonia to be released during the decomposition process in AlAB in agreement with the experimental results³¹. In addition, our observation that B-H populations are larger than N-H populations allows us to deduce that H(B) atom is detached from MABs prior to the H(N) atom in the process of the dehydrogenation.

Both the highest occupied molecular orbital (HOMO) and the lowest unoccupied molecular orbital (LUMO) play important roles in the chemical properties of the molecules. We calculated the HOMO-LUMO gaps for the three MABs and they are listed in Table 1. From the energy gaps, we predict the following trend of stability: $\text{MgAB} \approx \text{AlAB} > \text{CaAB}$. The calculated band gaps (listed in Table 1 as well) again predict the similar trend of stability and the insulating nature of examined MABs. One should keep in mind that band gaps or HOMO-LUMO gaps are not well described by GGA functionals (for example, PBE)⁵⁴. The description could be improved by using hybrid DFT functionals instead.

In a computational study on MABs ($\text{M}=\text{Li}, \text{Na}, \text{K}, \text{Be}, \text{Mg}, \text{Ca}, \text{Sr}, \text{Sc}$)²⁹ it has been reported that MABs become more stable as the metal cation moves down in the periodic table along a given column or as the metal cation moves to the left along a given row. Authors also predicted that MgAB is surprisingly more stable than CaAB (an exception to the rule), which is in agreement to our conclusion. Authors suggested that it is due to the fact that MgH_2 is much less stable than CaH_2 ²⁰.

3.2 Density of states (DOS)

The calculated total and partial electronic DOS for MgAB, CaAB and AlAB are shown in Fig. 2. In MgAB, in the lowest energy region there is one band of the energy ~ -40 eV which is composed of Mg $2p$ states. The next band of the energy ~ -15 eV is primarily composed of N $2s$ and H $1s$ states and has a very small contribution from B $2p$ and B $2s$ states. Such a big energy difference between these two bands indicates again that Mg-N bond is a pure ionic bond (see also the population discussion above). The valence band ($\sim -10 - 0$ eV) is composed of N $2p$, B $2s$, B $2p$ and H $1s$ states. The partial DOS of CaAB has a similar trend to that of MgAB. In the lowest energy region there are two bands of the energy of ~ -38 eV and ~ -20 eV which are accounted for by Ca $4s$ and $3p$ states, respectively. The next band of the energy ~ -15 eV has a very similar composition to that of MgAB (N $2s$ and H $1s$), however, the smaller energy difference between this band and the one of energy ~ -20 eV indicates a slight covalent character of Ca-N bonds. However, the partial DOS of AlAB looks much more different. The lowest energy band ~ -15 eV is dominated by N $2s$ states and H $1s$ states and has a very small contribution from Al $3s$ states and B $2s$ states. The valence band is not only composed of N $2p$, B $2s$, B $2p$ and H $1s$ states, but also of Al $3s$ and Al $3p$ states. The latter indicates a strong covalent character of Al-N bonds discussed above. The strong sp hybridization of states between N, B and H atoms in all the three MABs suggests a covalent nature of B-N, N-H and B-H bonds.

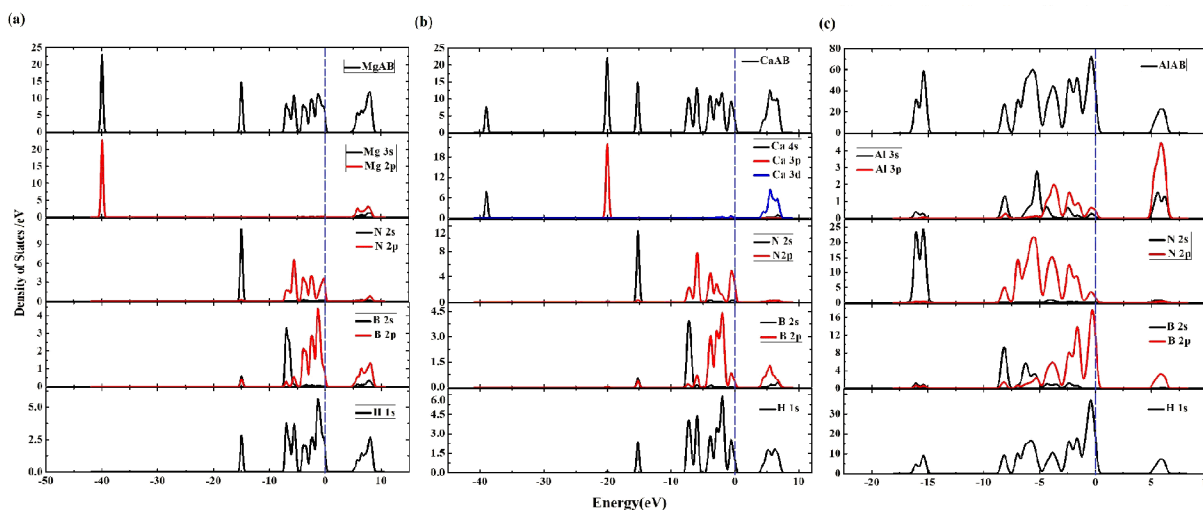


Fig. 2 Total and partial electronic DOS of (a) MgAB, (b) CaAB and (c) AlAB

3.3 Phonon DOS

In this section we discuss the vibrational modes (see Table 2) extracted from the calculated phonon DOS (see Fig. 3). First of all, one should notice that the translational lattice mode dominated by motion of metals (M) and the stretching modes of M-N and M-B are below 500cm^{-1} . In this region the number of vibrational modes in AlAB is larger than in MgAB and CaAB due to the lower geometric symmetry of AlAB (C_{3v}) compared to the other two (C_{2v}).

The B-N rotation modes are in the range of $500\text{-}900\text{ cm}^{-1}$, the N-B stretching mode is around $800\text{-}900\text{ cm}^{-1}$, BH_3 deformation mode (metal movement with H-B scissors mode) is in the range of $1110\text{-}1400\text{ cm}^{-1}$, the NH_3 deformation mode is around 1500 cm^{-1} , the B-H stretching mode is around $2100\text{-}2600\text{ cm}^{-1}$ and the N-H stretching mode is in the range of $3300\text{-}3600\text{ cm}^{-1}$. Importantly, our calculated frequencies are in a reasonable agreement with the experimental frequencies obtained from FTIR spectroscopy experiments on AlAB and $\text{Mg}(\text{NH}_2\text{BH}_3)\text{NH}_3$ ^{12,27}. The experimental N-H stretching frequencies are in the range of $3258\text{-}3302\text{ cm}^{-1}$ and B-H stretches in a range of $2875\text{-}2969\text{ cm}^{-1}$ and $2265\text{-}2358\text{ cm}^{-1}$. The shift to higher wavenumbers in the simulation most likely arises due to underestimation of electrostatic forces between the Al^{3+} and $[\text{NH}_2\text{BH}_3]^-$ groups.

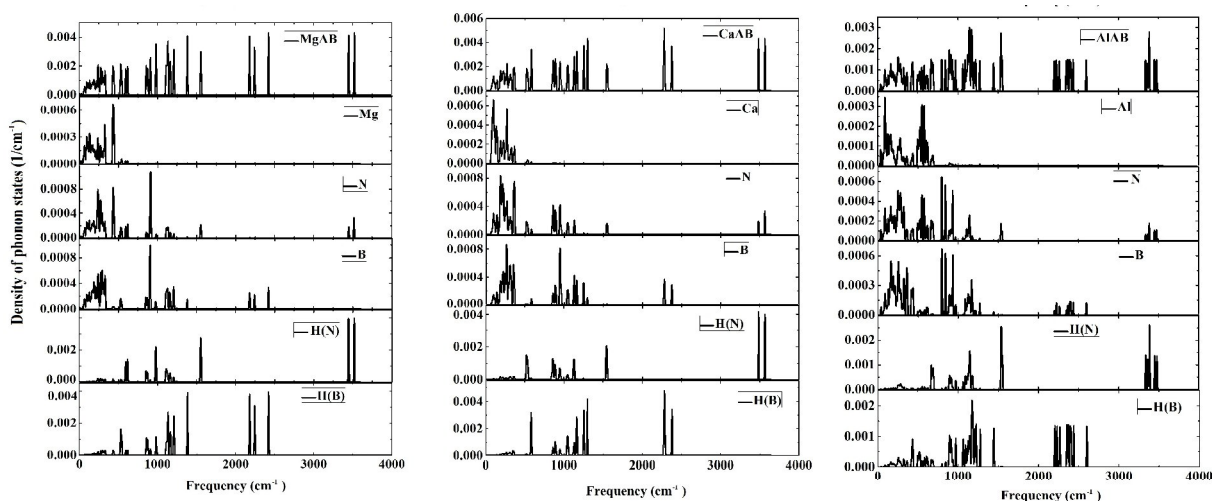


Fig. 3 Total and partial phonon DOS of (a) MgAB (b) CaAB and (c) AlAB

Table 2 Calculated vibrational modes of MgAB, CaAB and AlAB. The frequencies are in cm^{-1} .

Mode	MgAB	CaAB	AlAB
Lattice wagging	192-172	119-186	34-181
M-N stretching	194-272	199-255	189-211
M-B stretching	294-450	260-364	221-373
B-N rotation	525-856	513-587	412-692
N-B stretching	899-916	836-967	796-845

H(B), H(N) wagging	976-1130	1135-1124	880-1112
H-B scissors	1132-1386	1152-1298	1120-1273
H-N scissors	1548-1564	1540-1557	1443-1553
H-B stretching	2173-2423	2269-2377	2196-2603
H-N stretching	3446-3522	3485-3567	3337-3479

3.4 Thermodynamic properties

In order to examine thermodynamic properties of MABs (M = Mg, Ca, Al), we calculated enthalpies (H_m^\ominus), entropies (S_m^\ominus) and Gibbs free energies (G_m^\ominus) of these solid state compounds (see Fig. 4). As all these properties depend on the temperature, we can obtain the relationships between MABs' thermodynamic properties and temperature (see Eq. 3.4-1~3.4-3 and Table 3) and compare them for different MABs.

$$H_m^\ominus = A + BT + CT^2 \quad (3.4-1)$$

$$G_m^\ominus = A' + B'T + C'T^2 \quad (3.4-2)$$

$$S_m^\ominus = \frac{A''}{T} + B'' + C''T \quad (3.4-3)$$

Table 3 The relationship between MABs' thermodynamic properties and temperature

MAB	equation	MAB	equation
MgAB	$H_m^\ominus = -0.495 + 4.66 \times 10^{-3}T + 1.725 \times 10^{-5}T^2$	AlAB	$H_m^\ominus = -0.473 + 4.57 \times 10^{-3}T + 1.731 \times 10^{-5}T^2$
	$G_m^\ominus = 0.090 + 8.54 \times 10^{-4}T - 2.304 \times 10^{-5}T^2$		$G_m^\ominus = 0.086 + 8.69 \times 10^{-4}T - 2.305 \times 10^{-5}T^2$
	$S_m^\ominus = \frac{-0.585}{T} + 3.81 \times 10^{-3} + 4.029 \times 10^{-5}T$		$S_m^\ominus = \frac{-0.56}{T} + 3.70 \times 10^{-3} + 4.037 \times 10^{-5}T$
CaAB	$H_m^\ominus = -0.097 + 1.03 \times 10^{-3}T + 2.806 \times 10^{-5}T^2$		
	$G_m^\ominus = 0.032 + 1.52 \times 10^{-5}T - 4.092 \times 10^{-6}T^2$		
	$S_m^\ominus = \frac{-0.13}{T} + 1.05 \times 10^{-3} + 6.898 \times 10^{-6}T$		

Our results presented in Table 3 show that changes in entropy (S_m^\ominus), enthalpy H_m^\ominus and Gibbs free energy $G_m^\ominus = H_m^\ominus - TS_m^\ominus$ values due to changes in temperature are similar for both compounds, MgAB and AlAB, but differs for CaAB (A, A' or A'' values are much lower for CaAB than for

MgAB and AlAB, indicating smaller changes). The fact that CaAB has the highest enthalpy suggests that it also has the highest internal energy at 0K in this series of system. The latter leads to smallest entropy and free energy values. Thermodynamic properties seem to be very similar for AlAB and MgAB compounds. The changes in entropy and Gibbs free energies of MAB compounds increase with temperature due to the change of dominance of different vibration modes in low and high temperatures. The low frequency translation and rotation of the molecules are the dominant vibration modes at low temperature, whereas the high frequency vibration modes (inter- and intra-molecular) will start dominate at high temperatures.

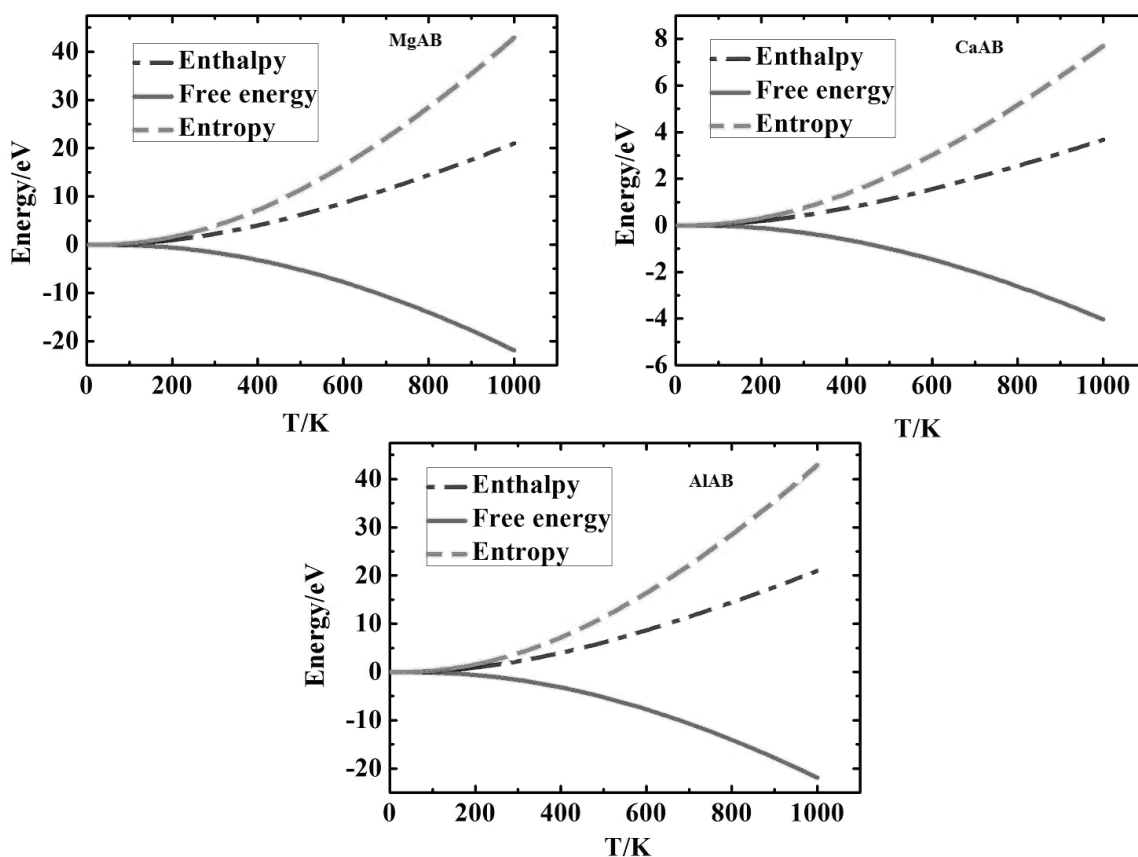


Fig. 4 The entropy, enthalpy and Gibbs free energy as a function of temperature T for MgAB, CaAB and AlAB.

3.5 Dynamic study of dehydrogenation

The dynamics study of dehydrogenation was performed on MABs in gas phase using the Gaussian 09 program package in order to obtain decomposition pathways. Our calculated barriers are relatively high. We believe that it is due the fact that our calculations were performed in gas phase and room temperature, whereas experiments²⁰⁻²⁶ were conducted on crystal MABs at around

100 °C. However, the calculated barriers can still help us to understand the dehydrogenation pathways and improve the hydrogenation storage properties of MABs.

Shimoda and Fijalkowski have recently shown that the major mechanism of decomposition in ABs is the direct evolution of hydrogen by $\text{N-H}^{\delta+} \dots \delta\text{-H-B}^{26, 55}$. Based on this, we propose direct dehydrogenation pathways for CaAB and MgAB (Eq. 3.5-1, Fig. 5) and AlAB (Eq. 3.5-2, Fig. 6).

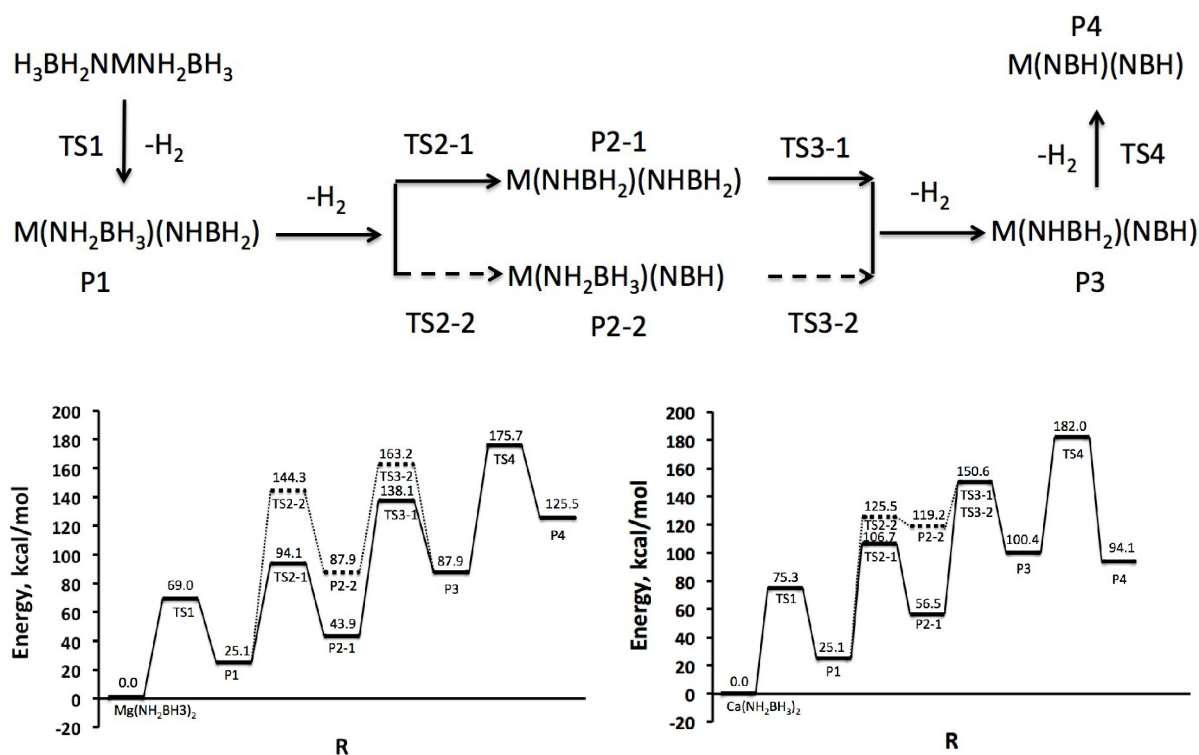
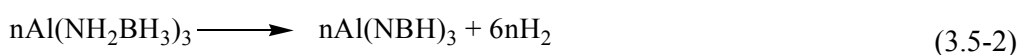
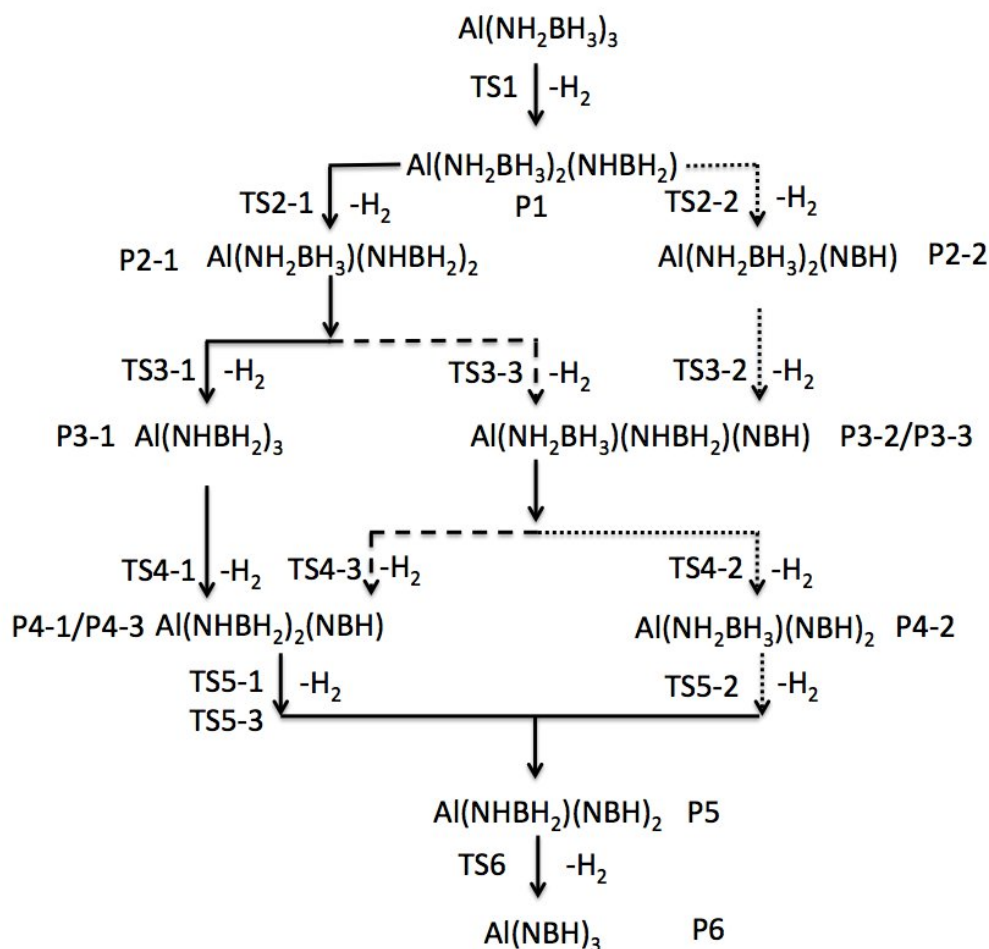


Fig. 5 Top: The flow charts of dehydrogenation for MgAB and CaAB. Bottom: The schematic energy profiles for the different paths of dehydrogenation of MgAB (left) and CaAB (right). PX-1 and PX-2 correspond to products in Path 1 and Path 2, respectively. TSX-1 and TSX-2 correspond to transition states in Path 1 and Path 2, respectively.

We determine two dehydrogenation paths (Path 1 and Path 2) for MgAB and CaAB and three dehydrogenation paths (Path 1, Path 2 and Path 3) for AlAB. The flow charts and the schematic energy profiles for consecutive dehydrogenation steps for the different paths of dehydrogenation are presented in Fig. 5 and Fig. 6. As the energy barrier for the 1st dehydrogenation step for AlAB (56.5 kcal/mol) is lower than for MgAB (69.0 kcal/mol) and CaAB (75.3 kcal/mol), AlAB will start releasing H_2 at lowest temperature. This is agreement with the experiments showing that AlAB will

start dehydrogenate at the temperature of 50°C¹⁸, whereas MgAB¹⁹ and CaAB²⁰ will start dehydrogenate at around 75°C and 90°C, respectively. The Path 1 seems to be the most probable pathway for CaAB and MgAB whereas the Path 1/Path 3 seem to be the most probable pathway for AlAB (that depends on the reaction conditions), indicating that dehydrogenation from the same AB group twice in a row is less likely to occur. The rate determining step for dehydrogenation of MgAB and CaAB (Path 1) is step Nr. 3 (energy barrier of 94.2 kcal/mol and 94.1 kcal/mol, respectively), whereas the rate determining step for dehydrogenation of AlAB (Path1/Path3) is the last step (energy barrier of 100.4 kcal/mol).



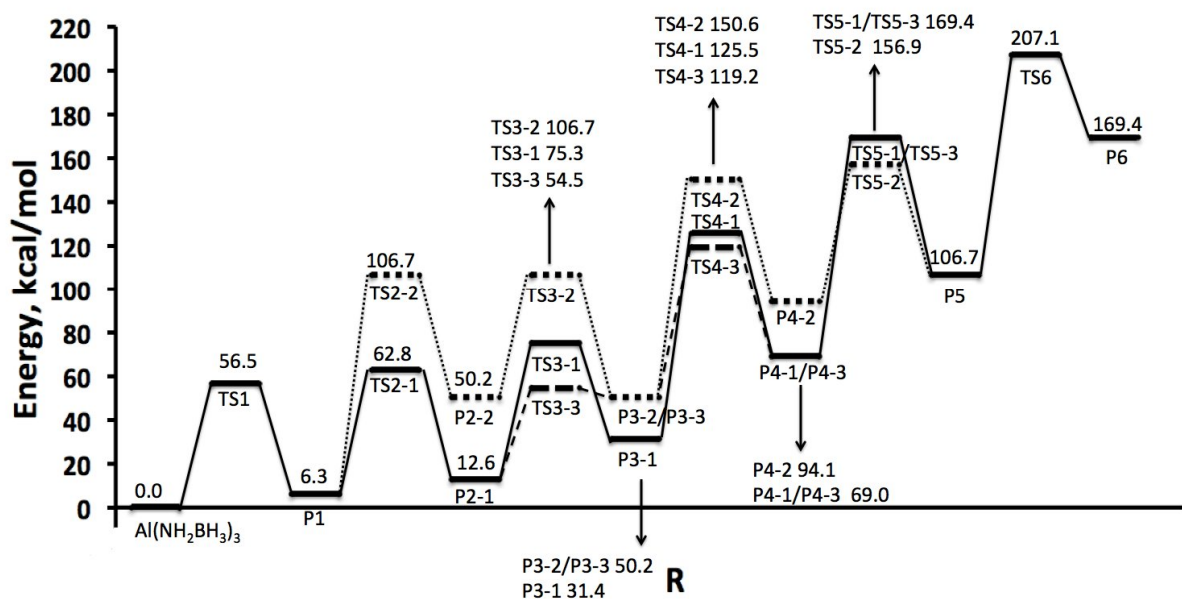


Fig. 6 Top: The flow charts of dehydrogenation for AlAB. Bottom: The schematic energy profiles for the different paths of dehydrogenation of AlAB. PX-1, PX-2 and PX-3 correspond to products in Path 1, Path 2 and Path 3, respectively. TSX-1, TSX-2 and TSX-3 correspond to transition states in Path 1, Path 2 and Path 3, respectively.

The determined energy barriers associated with dehydrogenation steps can be approximated to free energy barriers (ΔG^\ddagger) and thus can be related to the rate constants of dehydrogenation according to this equation:

$$\text{rate} = \kappa \frac{k_b T}{h} \times \exp\left(-\frac{\Delta G^\ddagger}{RT}\right), \quad 3.5-1$$

where κ is the transmission coefficient (assumed to be 1 in our case), k_b is the Boltzmann constant, R is the gas constant, h is the Planck constant and T is the temperature. This equation is valid only within the hypotheses of the Transition State Theory. It was shown experimentally¹⁸⁻²⁰ that all hydrogen ($4n$ H₂ from MgAB and CaAB and $6n$ from AlAB) can be released at the temperature of 400°C. The dehydrogenation rates at 400 °C can then be calculated by inserting energy barriers for rate determining steps (94.1 kcal/mol for MgAB, 94.1 kcal/mol for CaAB and 100.4 kcal/mol for AlAB) into Eq. 3.5-1. The calculated dehydrogenation rates follow the trend MgAB($1.73 \times 10^{-14} \text{ min}^{-1}$) \approx CaAB($1.72 \times 10^{-14} \text{ min}^{-1}$) $>$ AlAB($2.18 \times 10^{-16} \text{ min}^{-1}$).

4. Summary

We used the Monte Carlo simulations to simulate the crystal structures of MgAB and AlAB. Our first principle calculations of the electronic structure of crystal MABs (M = Mg, Ca, Al) revealed a covalent character of the Al – N (in particular) and Ca-N bonds in contrast to the ionic Mg-N bond. Furthermore, from the HOMO-LUMO gaps we predicted the following trend of stability: MgAB \approx AlAB > CaAB. From the phonon DOS analysis, we obtained the detailed vibrational modes of MABs and concluded that due to the lower geometric symmetry of AlAB in the frequency region (0 – 500 cm⁻¹) the number of vibrational modes in AlAB is larger than in MgAB and CaAB. Thermodynamic properties and their dependence on temperature seem to be very similar for AlAB and MgAB compounds and are larger than for CaAB. Our dynamic study of dehydrogenation revealed that AlAB will start releasing H₂ at the lowest temperature due to the lowest energy barrier for the 1st dehydrogenation step. Finally, we used the determined energy barriers for the rate determining steps of dehydrogenation to calculate the dehydrogenation rates at 400 °C – temperature at which all H₂ is released (4n H₂ from MgAB and CaAB and 6n H₂ from AlAB). The dehydrogenation rates follow the trend MgAB(1.73 \times 10⁻¹⁴ min⁻¹) \approx CaAB(1.72 \times 10⁻¹⁴ min⁻¹) > AlAB(2.18 \times 10⁻¹⁶ min⁻¹).

In order to better understand the decomposition mechanism of solid MABs we are currently performing Car-Parrinello molecular dynamics simulations at a variety of temperatures and pressures.

We believe that our findings on MABs (M=Mg, Ca, Al) is an important step in the ongoing development of MABs as hydrogen storage materials.

Acknowledgements

The authors acknowledge the financial support from the National Natural Science Foundation of China (NSFC 21071019) and the Program for New Century Excellent Talents in University (NCET-09- 0051). The authors are also grateful to Prof. John E. McGrady and Dihao Zeng (Department of Chemistry, Inorganic Chemistry Laboratory, University of Oxford) for helpful discussions.

References

1. Y. Zhang, K. J. Shimoda, T. Ichikawa and K. Y., *J. Phys. Chem. C*, 2010, **114**, 14662-14664.
2. T. Kar and S. Scheiner, *J Chem Phys*, 2003, **119**, 1473-1482.
3. A. C. Stowe, W. J. Shaw, J. C. Linehan, B. Schmid and T. Autrey, *Phys Chem Chem Phys*, 2007, **9**, 1831-1836.
4. Z. T. Xiong, Y. S. Chua, G. T. Wu, W. L. Xu, P. Chen, W. Shaw, A. Karkamkar, J. Linehan, T. Smurthwaite and A. T., *Chem Commun*, 2008, **43**, 5595-5597.
5. J. Demaison, J. Lievin, A. G. Csar and C. Gutle, *J Phys Chem A*, 2008, **112**, 4477-4482.
6. J. Dillen and P. Verhoeven, *J Phys Chem A*, 2003, **107**, 2570-2577.
7. Y. Meng, Z. Y. Zhou, C. S. Duan, B. Wang and Q. Zhong, *J Mol Struct*, 2005, **713**, 135-144.
8. M. Jacoby, *Chem Eng News*, 2004, **82**, 22-25.
9. D. Schneider, *Am Sci*, 2005, **93**, 1.
10. Q. A. Zhang, C. X. Tang, C. H. Fang, F. Fang, D. Sun, L. Z. Ouyang and M. Zhu, *J. Phys. Chem. C*, 2010, **114**, 1709-1714.
11. G. L. Xia, X. B. Yu, Y. H. Guo, Z. Wu, C. Z. Yang, H. K. Liu and S. X. Dou, *Chem-eur J*, 2010, **16**, 3763 - 3769.
12. J. H. Luo, X. D. Kang, Z. Z. Fang and P. Wang, *Dalton Trans.*, 2011, **40**, 6469-6474.
13. Yong Shen Chua, Hui Wu, Wei Zhou, Terrence J. Udovic, Guotao Wu, Zhitao Xiong, Ming Wah Wong and P. Chen, *Inorg Chem*, 2012, **51**, 1599-1603.
14. H. V. K. Diyabalanage, T. Nakagawa, R. P. Shrestha, T. A. Semelsberger, B. L. Davis, B. L. Scott, A. K. Burrell, W. I. F. David, K. R. Ryan, M. O. Jones and P. P. Edwards, *J Am Chem Soc*, 2010, **132**, 11836-11837.
15. Z. T. Xiong, C. K. Yong, G. T. Wu, P. Chen, W. Shaw, A. Karkamkar, T. Autrey, M. O. Jones, S. R. Johnson, P. P. Edwards and W. I. F. David, *Nature Materials*, 2008, **7**, 138-141.
16. D. J. Wolstenholme, K. T. Trabolsee, A. Decken and G. S. McGrady, *Organometallics*, 2010, **29**, 5769-5772.
17. F. H. Stephens, R. T. Baker and M. H. Matus, *Angew Chem Int Edit*, 2007, **46**, 746-749.
18. M. Frederick Hawthorne, Satish S. Jalisatgi and J. Wu, Chemical Hydrogen Storage Using Polyhedral Borane Anions and Aluminum-Ammonia-Borane Complexes.
19. J. Luo, X. Kang and P. Wang, *Energy Environ. Sci.*, 2013, **6**, 1018-1025.
20. Himashinie V. K. Diyabalanage, Roshan P. Shrestha, Troy A. Semelsberger, Brian L. Scott, Mark E. Bowden, Benjamin L. Davis and A. K. Burrell, *Angew Chem Int Edit*, 2007, **46**, 8995-8997.
21. M. Ramzan, F. Silvearv, A. Blomqvist, R. H. Scheicher, S. Lebegue and R. Ahuja, *Phys Rev B*, 2009, **79**, 1-3.
22. K. Wang, J. G. Zhang, T.-T. Man, M. Wu and C. C. Chen, *Chem. Asian J*, 2013, **8**, 1076 - 1089.
23. K. Wang, J. G. Zhang, T. T. Man, M. Wu, S. W. Zhang, T. L. Zhang and L. Yang, *Int J Quantum Chem*, 2013, **113**, 1358-1364.
24. C. Z. Wu, G. T. Wu, Z. T. Xiong, W. I. F. David, K. R. Ryan, M. O. Jones, P. P. Edwards, H. L. Chu and P. Chen, *Inorg Chem*, 2010, **49**, 4319-4323.
25. H. Wu, W. Zhou and T. Yildirim, *J Am Chem Soc*, 2008, **130**, 14834-14839.
26. K. Shimoda, K. Doi, T. Nakagawa, Y. Zhang, H. Miyaoka, T. Ichikawa, Masataka Tansho, T. Shimizu, A. K. Burrell and Y. Kojima, *J. Phys. Chem. C*, 2012, **116**, 5957-5964.
27. Y. S. Chua, G. T. Wu, Z. T. Xiong, A. Karkamkar, J. P. Guo, M. X. Jian, M. W. Wong, T. Autrey and P. Chen, *Chem Commun*, 2010, **46**, 5752-5754.
28. W. Li, G. Wu, Y. Chua, Y. P. Feng and P. Chen, *Inorg Chem*, 2011, **51**, 76-87.
29. Y. S. Zhang and C. Wolverton, *J. Phys. Chem. C*, 2012, **116**, 14224-14231.
30. C. B. Lingam, K. R. Babu, S. P. Tewari, G. Vaitheeswaran, S. Lebegue, *J. Phys. Chem. C*, 2011, **115**, 18795-18801.

31. M. F. Hawthorne, S. S. Jalisatgi, H. B. Lee and J. G. Wu, Chemical Hydrogen Storage Using Aluminum Ammonia-Borane Complexes, University of Missouri, 2010.
32. R. V. Genova, K. J. Fijalkowski, A. Budzianowski and W. Grochala, *J Alloy Compd*, 2010, **499**, 144-148.
33. Accelery, Polymorph Predictor <http://accelrys.com/products/datasheets/polymorph-predictor.pdf>. 2011
34. M. D. Segall, P. J. D. Lindan, M. J. Probert, C. J. Pickard, P. J. Hasnip, S. J. Clark and M. C. Payne, *J. Phys.: Condens. Matter*, 2002, **14**, 2717-2744.
35. M.J.T. Frisch, G. W.; Schlegel, H. B.; Scuseria, G. E.; Robb, M. A.; Cheeseman, J. R.; Montgomery, J. A.; Jr.; Vreven, T.; Kudin, K. N.; Burant, J. C.; Millam, J. M.; Iyengar, S. S.; Tomasi, J.; Barone, V.; Mennucci, B.; Cossi, M.; Scalmani, G.; Rega, N.; Petersson, G. A.; Nakatsuji, H.; Hada, M.; Ehara, M.; Toyota, K.; Fukuda, R.; Hasegawa, J.; Ishida, M.; Nakajima, T.; Honda, Y.; Kitao, O.; Nakai, H.; Klene, M.; Li, X.; Knox, J. E.; Hratchian, H. P.; Cross, J. B.; Bakken, V.; Adamo, C.; Jaramillo, J.; Gomperts, R.; Stratmann, R. E.; Yazyev, O.; Austin, A. J.; Cammi, R.; Pomelli, C.; Ochterski, J. W.; Ayala, P. Y.; Morokuma, K.; Voth, G. A.; Salvador, P.; Dannenberg, J. J.; Zakrzewski, V. G.; Dapprich, S.; Daniels, A. D.; Strain, M. C.; Farkas, O.; Malick, D. K.; Rabuck, A. D.; Raghavachari, K.; Foresman, J. B.; Ortiz, J. V.; Cui, Q.; Baboul, A. G.; Clifford, S.; Cioslowski, J.; Stefanov, B. B.; Liu, G.; Iashenko, A.; Piskorz, P.; Komaromi, I.; Martin, R. L.; Fox, D. J.; Keith, T.; Al-Laham, M. A.; Peng, C. Y.; Nanayakkara, A.; Challacombe, M.; Gill, P. M. W.; Johnson, B.; Chen, W.; Wong, M. W.; Gonzalez, C.; Pople, J. A., *Gaussian 09*, Wallingford, 2009.
36. K. Wang, J.-G. Zhang, T.-T. Man, M. Wu, S.-W. Zhang, T.-L. Zhang and L. Yang, *Int J Quantum Chem*, 2013, **113**, 1358–1364.
37. K. Wang, J.-G. Zhang, W. Yang, M. Wu, T.-T. Man, T.-L. Zhang and S.-W. Zhang, *Struct Chem*, 2013, **24**, 1527-1536.
38. M. H. Gordon, J. A. Pople and M. J. Frisch, *Chem Phys Lett*, 1988, **153**, 503-506.
39. C. Lee, W. T. Yang, R. G. Parr *Phys. Rev. B*, 1988, **37**, 785–789.
40. A. D. Becke, *Phys. Rev. A*, 1988, **38**, 3098–3100.
41. V. K. Belsky and P. M. Zorkii, *Acta Crystallogr Sect A*, 1977, **33**, 1004-1006.
42. A. K. Rappé, C. J. Casewit, K. S. Colwell, W. A. Goddard and W. M. Skiff, *J. Am. Chem. Soc.*, 1992, **114**, 10024-10039.
43. P. Hohenberg and W. Kohn, *Phys Rev B*, 1964, **136**, 864-871.
44. W. Kohn and L. Sham, *Phys. Rev. A*, 1965, **140**, 1133-1138.
45. P. E. Blochl, *Phys Rev B*, 1994, **50**, 17953-17979.
46. J. P. Perdew and Y. Wang, *Phys. Rev. B*, 1992, **45**, 13244-13249.
47. J. P. Perdew, K. Burke and M. Ernzerhof, *Phys. Rev. Lett.*, 1996, **77**, 3865-3868.
48. D. Vanderbilt, *Phys. Rev. B* 1990, **41**, 7892-7895.
49. H. J. Monkhorst and J. D. Pack, *Phys. Rev. B* 1976, **13**, 5188-5192.
50. T. H. Fischer and J. Almlof, *J. Phys. Chem.*, 1992, **96**, 9768–9774.
51. Accelery, Polymorph Predictor <http://accelrys.com/products/datasheets/materials-studio-overview.pdf> 2011
52. R. J. Bartlet, D. P. George, *Int. J. Quantum Chem*, 1978, **14**, 561-581.
53. H. Wu, W. Zhou, F. E. Pinkerton, M. S. Meyer, Q. R. Yao, S. Gadipelli, T. J. Udovic, T. Yildirim and J. J. Rush, *Chem Commun*, 2011, **47**, 4102-4104.
54. S. M. Lee, X. D. Kang, P. Wang, H. M. Cheng and Y. H. Lee, *Chemphyschem*, 2009, **10**, 1825-1833.
55. K. J. Fijalkowski, R. Jurczakowski, W. K. m. ski and W. Grochala, *Phys Chem Chem Phys*, 2012, **14**, 5778–5784.